A Vector Magnetization Model for Single Crystal Based on Magnetic Domain Theory

Yating Li[1,2], Jun Liu[2], Yongjian Li[1*], Shuaichao Yue[1], Ruiying Chen[3], Christopher Harrison[2], Philip Anderson[2]
[1] State Key Laboratory of Intelligent Power Distribution Equipment and System, Hebei University of Technology, Tianjin 300401, China
[2]School of Engineering, Cardiff University, Cardiff, CF24 3AA, U.K,
[3]Department of Electrical Engineering, Tsinghua University, Beijing 100190, China

This paper presents an anisotropic anhysteresis magnetization model that incorporates both the evolution of elementary magnetic domains and the influence of crystallographic orientation. Under low field conditions, the domain distribution is determined based on the assumption that domains are confined to crystallographic easy axes. To capture the domain rotation behavior observed at higher fields, an additional easy state aligned with the external magnetic field direction is introduced. The high field domain configuration is obtained by minimizing the total free energy. The model enables quantitative analysis of 180° and 90° domain wall motion, as well as domain rotation based on elementary domain distributions. Preliminary verification of the proposed model is provided through comparisons with experimental measurements of grain oriented electrical steel under various magnetization directions, demonstrating its ability to characterize the anisotropic magnetization behavior of textured magnetic materials.

***Index Terms*—Magnetic anisotropy, magnetic permeability, magnetic materials, single crystal**

I. Introduction

The magnetic properties of grain-oriented (GO) electrical steels, such as permeability and iron losses, exhibit significant anisotropy. Such macroscopic anisotropy arises primarily from intrinsic magnetocrystalline anisotropy of iron-silicon crystals, associated with the easy axes in the <100> crystal directions and the pronounced crystallographic texture of the material [1]. Therefore, to accurately model the anisotropic behavior of electrical steels, it is essential to develop models that incorporate the crystallographic orientation of individual grains and capture their intrinsic magnetic anisotropy [2, 3].

The commonly used vector hysteresis models, such as the Jiles-Atherton model [4] and the dry friction model [5], begin with the modeling of the anhysteretic magnetization curve. As the backbone of these models, the anhysteretic magnetization curve largely dictates the shape of the hysteresis loops and influences the anisotropic properties of the model. The vectorization of anhysteretic magnetization modeling can be achieved by combining the scalar anhysteretic curves along the rolling and transverse directions, as in the elliptical model [6]. However, such an approach fails to capture the biaxial anisotropy of electrical steel, which arises from the Goss texture. To overcome the limitation, the tensorial permeability microstructure model is proposed to quantitatively predict effective permeability tensors by incorporating crystallographic texture, grain size and domain configuration [7]. However, this model is applicable under low-field conditions, where the magnetization of each domain remains aligned with the easy axes. To further improve computational efficiency and facilitate practical applications, a scalar permeability finite element microstructure model is proposed in [8] to predict anisotropic permeability, and is compared with the tensorial model. [9] captures anisotropy by decomposing magnetostriction into domain wall motion and rotation contributions and coupling the result with a JA–Preisach hybrid model. However, the model parameters depend on the magnetic-flux-density amplitude. From the perspective of energy-based homogenization, a multiscale model provides a link between macroscopic phenomenological descriptions and microscale micromagnetic simulations [10, 11]. A magneto-elastic model is developed for single crystals and then extended to polycrystalline materials via a multiscale homogenization approach, which is further adapted to account for hysteresis effects in [12]. Another analogous multiscale approach called the assembled domain structure model is constructed from a simplified domain structure model (SDSM) formed by six domains. The magnetization state is calculated by energy minimization of a SDSM particle [13]. Within the multiscale framework, [14] introduces hysteresis from domain theory by adding a hysteresis energy density to the free energy of each domain. [15] develops a micromagnetic method with large cells to simulate domain structures and anisotropy at much lower cost. The micromagnetic model captures the complex anisotropy from crystallographic texture and multiaxial stress, while the evolution of the magnetic domain distribution during magnetization was not analyzed. The energetic model establishes a relationship between the domain distribution and magnetization within the reversible field part for GO. However, its validity is limited to specific magnetization directions [16].

This paper proposes a vector anhysteretic model based on magnetic domain theory that accounts for crystallographic orientation. It extends the tensorial permeability model [7], which was capable of predicting anhysteretic behavior at small fields, to cover the full range of fields up to saturation. The model further leverages its magnetic domain theory foundation

Manuscript received April 1, 2015; revised May 15, 2015 and June 1, 2015; accepted July 1, 2015. Date of publication July 10, 2015; date of current version July 31, 2015. (Dates will be inserted by IEEE; "published" is the date the accepted preprint is posted on IEEE Xplore®; "current version" is the date the typeset version is posted on Xplore®). Corresponding author: Yongjian Li (e-mail: liyongjian@hebut.edu.cn).

Color versions of one or more of the figures in this paper are available online at http://ieeexplore.ieee.org.

Digital Object Identifier (inserted by IEEE).

to quantitatively describe elementary domain distributions and link them to potentially observable magnetic domain processes. The proposed model is demonstrated through comparisons with experimental results under various magnetization directions.

II. Model

Based on the assumption proposed by Bozorth [17], a cubic crystal is composed of a large number (N) of elementary magnetic domains with equal size. They can only orient along one of the easy axes, denoted as N_i (i=1-6). The number of domains oriented in the [100] direction is N_1, for the domains oriented in $[\bar{1}00]$ it is N_2, for the domains oriented in [010] it is N_3, for the domains oriented in $[0\bar{1}0]$ it is N_4, etc., as shown in Fig.1 (a). At the demagnetized state, the domains orientate along the six easy directions with equal probability. When an external magnetic field is applied, the number of the domain across the six easy axes — collectively referred to as domain configuration — will redistribute so that the resulting magnetization must have a component along the given field direction. After the magnetization of the crystal has increased to the point where the domain magnetization directions align with the cubic axes most closely aligned with the external magnetic field, Bozorth's assumption no longer holds. Beyond this point, the domains are allowed to rotate toward the field direction, at which point the additional easy state N_7 is introduced to represent this rotation.

A. Model I: The anhysteresis magnetization modeling under low field

Based on the Heisenberg possibility function, the most probable N_i is mathematically solved by [17]:

$$\begin{aligned} N_1 &= e^{\alpha+\beta\gamma_x} \quad N_3 = e^{\alpha+\beta\gamma_y} \quad N_5 = e^{\alpha+\beta\gamma_z} \\ N_2 &= e^{\alpha-\beta\gamma_x} \quad N_4 = e^{\alpha-\beta\gamma_y} \quad N_6 = e^{\alpha-\beta\gamma_z} \end{aligned}, \tag{1}$$

where γ_x, γ_y and γ_z are the direction cosines of $\boldsymbol{H}$ in the crystal coordinate system (CCS), α and β are obtained by:

$$\frac{\gamma_x sh(\gamma_x\beta)+\gamma_y sh(\gamma_y\beta)+\gamma_z sh(\gamma_z\beta)}{ch(\gamma_x\beta)+ch(\gamma_y\beta)+ch(\gamma_z\beta)} = \frac{B_\mathrm{h}}{B_\mathrm{s}}, \tag{2}$$

where B_h is the magnetization component along the applied magnetic field. The magnetic flux density $\boldsymbol{B}$ in the CSS is determined using the following equation:

$$\boldsymbol{B} = \begin{bmatrix} B_x \\ B_y \\ B_z \end{bmatrix} = \begin{bmatrix} (N_1-N_2)B_\mathrm{s}/N \\ (N_3-N_4)B_\mathrm{s}/N \\ (N_5-N_6)B_\mathrm{s}/N \end{bmatrix}, \tag{3}$$

where B_x, B_y, and B_z are the components of $\boldsymbol{B}$ along the x-, y-, and z- axes, B_s is the saturation magnetic flux density.

The distribution of N_i (i=1-6) should satisfy the following constraints:

$$N_1+N_2+N_3+N_4+N_5+N_6 = N, \tag{4}$$

$$\boldsymbol{B} = \mu_0\boldsymbol{\mu}\boldsymbol{H}. \tag{5}$$

The sum of the calculated N_i (i=1-6) equals the constant N, as expressed in (4). The calculated magnetic flux density $\boldsymbol{B}$, the applied magnetic field $\boldsymbol{H}$, and relative permeability tensor $\boldsymbol{\mu}$ satisfy the constitutive relation given in (5). μ_0 is the vacuum permeability. The permeability tensor $\boldsymbol{\mu}$, considering the crystallographic texture and domain configuration in CSS, is expressed as [7]:

$$\boldsymbol{\mu} = \frac{1}{N}\sum_{i=1}^{6} N_i\boldsymbol{\mu}_i, \tag{6}$$

where $\boldsymbol{\mu}_i$ is the elementary permeability tensors for domains along easy axes, defined as:

$$\begin{aligned} \boldsymbol{\mu}_1 &= \boldsymbol{\mu}_2 = diag(\mu_c,1,1) \\ \boldsymbol{\mu}_3 &= \boldsymbol{\mu}_4 = diag(1,\mu_c,1), \\ \boldsymbol{\mu}_5 &= \boldsymbol{\mu}_6 = diag(1,1,\mu_c) \end{aligned} \tag{7}$$

where diag(·) represents a diagonal matrix with the given elements on its main diagonal, μ_c is the relative elementary permeability of a domain oriented along the six easy axes. The permeability tensor in sample coordinate system (SCS) is $\boldsymbol{g}^{-1}\boldsymbol{\mu}\boldsymbol{g}$, where $\boldsymbol{g}$ is the crystal orientation matrix. The proposed model is capable of predicting the anhysteretic magnetization curve of polycrystalline materials through the ODF, while this paper focuses on the single crystal case. GO is selected as the representative material because it exhibits a highly pronounced Goss texture. In GO steel, grain orientations typically deviate by only 5-8 ° from the ideal Goss direction, causing the material to behave similarly to a Goss single crystal in terms of magnetic anisotropy [18]. Therefore, applying the single crystal model to GO steel provides a valid approximation for evaluating its magnetic properties.

The above model is only valid up to a certain field strength, depending on the direction of the applied magnetic field. This limitation arises because the model considers only the effect of magnetocrystalline anisotropy, restricting the variation in magnetic domain distributions to the six easy axes, whose unit vectors are denoted as $\boldsymbol{e}_i$ (i=1-6). As the external magnetic field $\boldsymbol{H}$ increases, the magnetic domains tend to align with the easy axes closest to the direction of $\boldsymbol{H}$, resulting in the maximum magnetic flux density $\boldsymbol{B}_\mathrm{max}$. There are only three limiting cases. First, a single easy direction is closest to $\boldsymbol{H}$. Second, two easy directions are equally closest to $\boldsymbol{H}$. Third, all three easy directions are equally closest to $\boldsymbol{H}$. In the case of GO and in-plane directions, when $\boldsymbol{H}$ is applied along the RD, the magnetic domains eventually align entirely along the $\boldsymbol{e}_1$ direction as $\boldsymbol{H}$ increases. The limiting domain configuration is $\boldsymbol{N}_\mathrm{lim}$= [$N$,0,0,0,0,0], thus $\boldsymbol{B}_\mathrm{max} = B_\mathrm{s}\boldsymbol{e}_1$. When $\boldsymbol{H}$ is applied at 55° to RD, i.e. the <111> direction (see Fig. 2) the domains align equally among $\boldsymbol{e}_1$, $\boldsymbol{e}_3$ and $\boldsymbol{e}_5$, giving $\boldsymbol{N}_\mathrm{lim}$=[$N$/3,0,$N$/3,0,$N$/3,0], thus $\boldsymbol{B}_\mathrm{max} = (1/\sqrt{3})B_\mathrm{s}\boldsymbol{e}_H$ .When $\boldsymbol{H}$ is applied along the TD, the resulting domain configuration becomes $\boldsymbol{N}_\mathrm{lim}$=[0,0,$N$/2,0,$N$/2,0], thus $\boldsymbol{B}_\mathrm{max} = (1/\sqrt{2})B_\mathrm{s}\boldsymbol{e}_H$. The component of $\boldsymbol{B}_\mathrm{max}$ along the direction of $\boldsymbol{H}$, denoted as B_maxh, is calculated by:

$$B_\mathrm{maxh} = B_\mathrm{s}\boldsymbol{e}_{index}\cdot\boldsymbol{\gamma}, \tag{8}$$

where $\boldsymbol{e}_{index}$ is the easy axis direction that is closest to the direction of $\boldsymbol{H}$, $\boldsymbol{\gamma} = [\gamma_x\ \gamma_y\ \gamma_z]$ is the direction cosines of the $\boldsymbol{H}$ in the CCS. The ratio $B_\mathrm{maxh}/B_\mathrm{s}$ exhibits anisotropy as illustrated in Fig.1 (b).

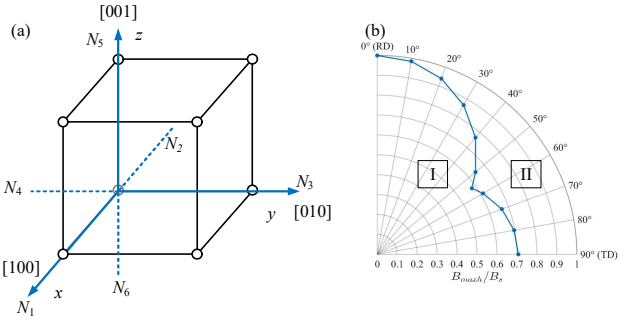

Fig.1. (a) Magnetic domain distribution in crystal ([100], [010], [001]); (b) The anisotropy of B_{hmax}/B_s.

B. The determination of the critical field $\boldsymbol{H}_{c1}$

Since Model I is only valid in Region I as shown in Fig.1 (b), the corresponding critical field $\boldsymbol{H}_{c1}$, representing the end of the Model I, can be determined accordingly. In Model I, the magnetic domain distribution $\boldsymbol{N}_{lim}$ is known, which allows for the calculation of the $\boldsymbol{B}_{max}$. Based on (6), the associated permeability $\boldsymbol{\mu}_{lim}$ can be derived from $\boldsymbol{N}_{lim}$, thereby enabling determination of the critical field $\boldsymbol{H}_{c1}$. As discussed in Section A, within the angular range of 0°-90° in the sample coordinate system of GO, the limiting magnetic domain configuration $\boldsymbol{N}_{lim}$ exhibits three representative cases. For a given external magnetic field $\boldsymbol{H}$ in different directions, the switch boundary between Region I and II is determined by comparing the component of $\boldsymbol{H}$ projected onto the nearest easy axis with the critical field $\boldsymbol{H}_{c1}$, as summarized in Table I.

TABLE I
THE CRITICAL FIELD $\boldsymbol{H}_{c1}$ OF GO UNDER IN-PLANE MAGNETIZATION ALONG DIFFERENT DIRECTIONS

Cases	$\boldsymbol{N}_{lim}$	Region Transition
$\phi \in [0°, 55°)$	$[N,0,0,0,0,0]$	$\lvert\boldsymbol{H}\rvert > \dfrac{\lvert\boldsymbol{H}_{c1}\rvert}{\gamma_x}$
$\phi = 55°$	$[N/3,0,N/3,0,N/3,0]$	$\lvert\boldsymbol{H}\rvert > \lvert\boldsymbol{H}_{c1}\rvert$
$\phi \in (55°, 90°]$	$[0,0,N/2,0,N/2,0]$	$\lvert\boldsymbol{H}\rvert > \dfrac{\lvert\boldsymbol{H}_{c1}\rvert}{\sqrt{2}\gamma_y}$

C. Model II: The anhysteresis magnetization modeling under high field

The assumption that the elementary domains are only allowed to orientate in the six easy directions does not apply any longer in Region II, as shown in Fig. 1(b), where energy due to the external field, Zeeman energy, outweighs the magnetocrystalline energy and needs minimizing. To account for the increasing influence of Zeeman energy on the magnetic domain distribution near saturation, an additional *easy* state is introduced, aligned with the direction of the applied magnetic field $\boldsymbol{H}$. The magnetic domain distribution along this axis is denoted as N_7. At this stage, the magnetization process is primarily governed by the rotation of domains from $\boldsymbol{e}_1$ through $\boldsymbol{e}_6$ toward $\boldsymbol{e}_7$. For crystals with Goss texture, the assumed orientations of the easy axes and the associated coordinate system are illustrated in Fig. 2.

The distribution of N_i (i=1-7) is determined by minimizing the total energy E_{min}, which comprises the Zeeman energy E_z and the magnetocrystalline anisotropy energy E_c, and is expressed as:

$$\begin{aligned} E_c &= K_0 + K_1(b_x^2 b_y^2 + b_y^2 b_z^2 + b_y^2 b_z^2) + K_2 b_x^2 b_y^2 b_z^2 \\ E_z &= -B_s H(b_x\gamma_x + b_y\gamma_y + b_z\gamma_z) \\ E_{min} &= E_c + E_z \end{aligned} \quad , \qquad (9)$$

where K_0, K_1, and K_2 are the anisotropy constants, b_x, b_y and b_z are the direction cosines of $\boldsymbol{B}$ in CCS. The magnetic flux density in CSS $\boldsymbol{B}$ is determined by:

$$\boldsymbol{B} = \begin{bmatrix} B_x \\ B_y \\ B_z \end{bmatrix} = \begin{bmatrix} (N_1 - N_2 + N_7\gamma_x)B_s / N \\ (N_3 - N_4 + N_7\gamma_y)B_s / N \\ (N_5 - N_6 + N_7\gamma_z)B_s / N \end{bmatrix}. \qquad (10)$$

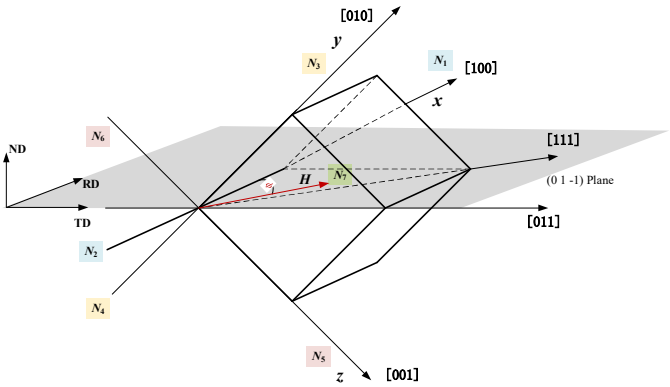

Fig.2. The orientation of iron crystals in Goss texture and the coordinate system used for the calculations.

In the process of minimizing the total energy, the initial domain configuration is set as $\boldsymbol{N}_{lim}$ and N_7 = 0, which corresponds to the domain distribution obtained at the end of Model I. The initial value selection in Model II is in essence the same as that used in [19] for directly determining the magnetization direction through energy minimization.

In Model II, the demagnetizing energy is neglected. This simplification is a good approximation under high-field conditions, where the Zeeman energy and magnetocrystalline anisotropy energy dominate the magnetization behavior. However, at low fields, the contribution of demagnetizing energy becomes significant. Accurately accounting for it requires micromagnetic modeling, which in turn demands knowledge of the spatial distribution of magnetic domains. The Bozorth model is based on the assumption of equally probable domain distributions along the six easy axes. Since the probability of alignment along N_7 is not known as a priori, it cannot be directly included in the probabilistic framework.

III. APPLICATION

A. Experimental system

A B27R090 GO electrical steel sheet of 0.27 mm in thickness is utilized to verify the present model. Disk specimen of 80 mm in diameter were prepared for magnetic measurements. Magnetic properties, including hysteresis loops and magnetization curves were measured using an in-house 2-D measurement system, as illustrated in Fig. 3(a). The measurements were carried out at a relatively low frequency, 20

Hz, to keep the classical eddy-current loss low while ensuring a stable signal of B and H. A detailed description of the measurement setup can be found elsewhere [20]. Experimental data obtained under uniaxial excitation in different directions are used in this paper to preliminarily demonstrate the capability of the proposed model to capture magnetic anisotropy. An example of the dataset is presented in Fig. 3(b).

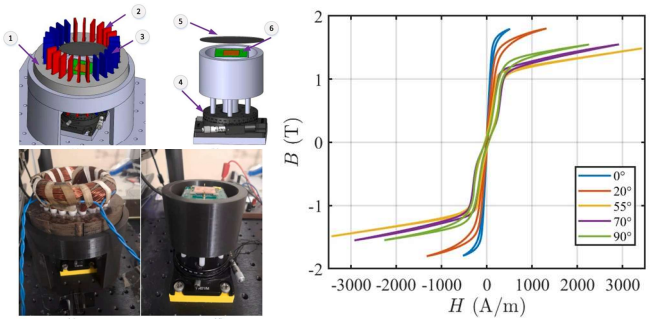

Fig.3. (a) 2-D measurement system. 1 Magnetising yoke. 2 x direction magnetising winding. 3 Un-energised y direction magnetising winding. 4 Angular adjustment. 5 Circular sample. 6 *B- H* sensor. (b) Hysteresis loops measured under uniaxial excitation along different directions.

B. Identification of the Parameters

The model parameters, including μ_c, K_0, K_1, and K_2, are identified by minimizing the average norm of the residual over all measured data. The anhysteretic magnetization curves are obtained from averaging the ascending and descending branches of the hysteresis loops measured in the RD (0°), TD (90°), and 55°. The identified parameters are then used to predict the anhysteresis curves in other directions to compare with the measurements. The objective function is defined as the absolute error between the calculated and experimental B_h values in the three directions:

$$\mathrm{RSS}=\frac{1}{3}\frac{1}{N}\sum_{j=1}^{3}\sum_{n=1}^{N_d}\left\|\frac{(\boldsymbol{B}_c^{n,j}\cdot\boldsymbol{H}^{n,j})}{\left\|\boldsymbol{H}^{n,j}\right\|^2}\boldsymbol{H}^{n,j}-\boldsymbol{B}_m^{n,j}\right\|. \qquad (11)$$

where N_d is the number of data points, and $\boldsymbol{B}_m$ and $\boldsymbol{B}_c$ are the measured and calculated magnetic flux density. The parameter μ_c influences the magnetic permeability in the low magnetic field region of the magnetization curve, whereas the coefficients K_0, K_1 and K_2 determine anisotropic behavior under high magnetic fields. The measured and calculated anhysteresis curves along three directions are shown in Fig. 4. The modeling results capture the qualitative trend of anisotropy: the permeability is highest along RD, lowest at 55°, and intermediate along TD. Discrepancies between predictions and measurements arise from both modeling and experimental factors. In the experimental data, a crossover appears in medium fields, indicating that the trend in the low field differs from that in the high field due to residual stress from the coating. At low fields, the stress effect dominates over crystallographic orientation. This stress enhances performance along RD but significantly reduces permeability along TD [21], leading to pronounced low field differences among the three directions. In addition, the experimental data used for trend validation are the midlines of the hysteresis loops as an approximation, which still differ from the true anhysteretic magnetization curve of a single crystal. At present, measurements of the anhysteretic magnetization curve of a single crystal are not available in this study. The steps arise from the transition between two modeling regimes with different underlying assumptions and are expected to be smoothed by polycrystalline model, as indicated by our preliminary work in [7, 8]. To reduce the discontinuity at the regime transition, we adjust the critical field to the intersection of the two magnetization curves, defined as H_{c2}. The critical field from the original criterion is used as a starting value for this adjustment. The calculated results are shown as a solid line in Fig. 4.

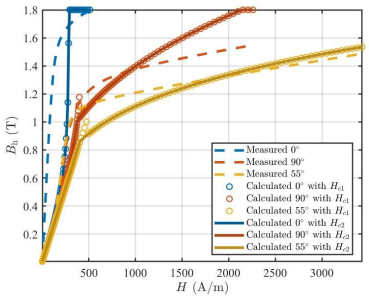

Fig.4. Measured and calculated anhysteresis curves under 0°, 55° and 90° excitations. (μ_c=7.43×10^3, K_0=0 J/m^3, K_1=3.86×10^3 J/m^3, K_2=2.99×10^4 J/m^3).

C. Validation and discussion of the Model

Fig. 5 shows the evolution of the domain distribution from N_1 to N_7 under uniaxial magnetic excitations along 0°, 55°, and 90° directions as a function of magnetic field strength. At 0°, where the field aligns with one of the easy directions $\boldsymbol{e}_1$, N_1 increases monotonically with the applied field at the expense of N_2 through N_6. At 55°, N_1, N_3, and N_5 increase at the expense of N_2, N_4, and N_6. Once the distribution reaches $\boldsymbol{N}_{\mathrm{lim}}$, N_7 begins to increase, indicating the onset of domain rotation. Under 90° excitation, N_3 and N_5 grow at the expense of N_1, N_2, N_4, and N_6. Upon reaching $\boldsymbol{N}_{\mathrm{lim}}$, N_7 increases, reflecting a transition in the magnetization mechanism from domain wall motion to domain rotations. Due to the symmetry inherent in the configuration illustrated in Fig. 2, the Goss texture satisfies N_3=N_5 and N_4=N_6.

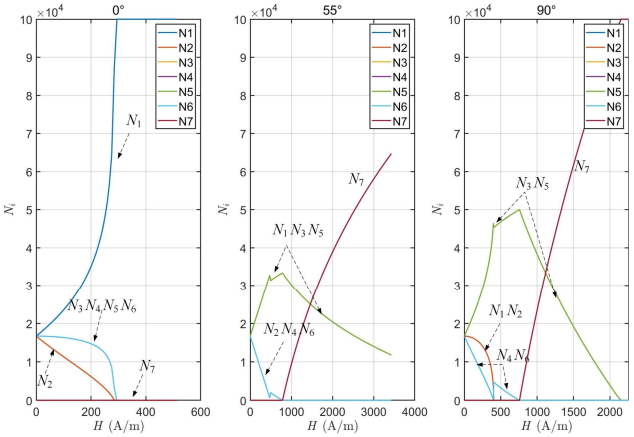

Fig.5. Domain distribution evolution under 0°, 55°, and 90°excitations.

Although the present model does not predict the domain patterns, further analysis of the statistical domain configurations, together with well-established principles in domain theory, provides valuable insight into the domain

processes and hence the underlying magnetization mechanisms. At the demagnetized state, domains are expected to form antiparallel domains equally distributed across three pairs of easy directions. N_{100}, N_{010}, and N_{001} represent the volume fraction of each antiparallel pair of easy axes. ΔN_{100}, ΔN_{010}, and ΔN_{001}, are defined in (12).

$$\begin{aligned} N_{100} &= (N_1 + N_2)/N \quad \Delta N_{100} = |N_1 - N_2|/N \\ N_{010} &= (N_3 + N_4)/N \quad \Delta N_{010} = |N_3 - N_4|/N \\ N_{001} &= (N_5 + N_6)/N \quad \Delta N_{001} = |N_5 - N_6|/N \end{aligned} \tag{12}$$

As an external magnetic field is applied, domains will rearrange themselves through domain processes including typically 180° and 90° domain wall motion and domain rotation towards the applied field direction. Increase of, say, N_1 at the expense of N_2, with N_{100} being nearly constant, would be manifested as 180° domain wall motion of those <100> domains. ΔN_{100}, ΔN_{010}, and ΔN_{001} quantify the imbalance within each antiparallel pair. $|N_{100}- N_{010}|$, $|N_{010}- N_{001}|$ and $|N_{100}- N_{001}|$ characterize the reorientation between orthogonal easy axes. For instance, the increase of $N_{100}- N_{010}$ would be consistent with N_{010} domains flipping to $N_{100,}$ through the motion of 90° domain walls. It is worth noting that due to the crystallographic symmetry of the Goss structure, $|N_{010}- N_{001}|$ remains zero throughout the magnetization process. Finally, the change of N_7 represents domain rotation towards or away from the applied field direction.

Fig. 6 juxtaposes the evolution of N_i (i=1-7) (left ordinate) with B_h (right ordinate), thus illustrating their correspondence to the anhysteretic curve under various excitation conditions. The adjusted critical field is the transition point between two models. The proportions of N_{100}, N_{010}, and N_{001} are stacked in the shaded region in the figure. For field directions in the [0°, 55°) region, as shown in Fig. 6 (a) - (c), the initial state of the region $H < H_{c2}$ is primarily governed by 180° domain-wall motion of the <100> domains in particular, as evidenced by ΔN_{100} increasing continuously. There is a slight increase of 180° domain wall motion of the <001> domains, as indicated by the ΔN_{001} rising slowly with the applied field. At the same time, the minor rise in $|N_{100}- N_{010}|$ and $|N_{100}- N_{001}|$ and the continuous increase of N_{100} evidence 90° wall motions, which would be consistent with the growth of closure domains accommodating the dominating 180° domain wall motion of those <100> domains. In consequence, the initial slope of the anhysteretic curve is modest. As the field increases, N_{010} and N_{001} decrease, the contribution of the 90° wall motion grows, yielding a steeper anhysteretic curve. Once $H \geq H_{c2}$, N_7 increases at the expense of what is left of the N_1, thus the anhysteretic curve approaches a plateau. In the 55° direction, the applied field makes an equal angle with $\boldsymbol{e}_1$, $\boldsymbol{e}_3$ and $\boldsymbol{e}_5$, so that N_{100}=N_{010}=N_{001} at all times, as shown in in Fig.6 (d). ΔN_{100}, overlapping with ΔN_{010} and ΔN_{001}, increases continuously. Meanwhile, $|N_{100}- N_{010}|$, $|N_{010}- N_{001}|$ and $|N_{100}- N_{001}|$ remain zero. It follows that the magnetization is driven by 180° domain wall motion equally in <100>, <010> and <001> domains, the averaging effect of which accounts for the slow or *hard* magnetisation and hence lower permeability. Above H_{c2}, domain rotation again dominates, leading to a simultaneous decrease in all three easy axes components while their relative proportions remain balanced. For field orientations in the range (55°, 90°] as shown in Fig.6 (e) and (f), the situation is the complementary case. The initial state of the region $H < H_{c2}$ is governed 180° domain wall motion of the <010> and <001> domains, as evidenced by overlapped ΔN_{010} and ΔN_{001} increasing. A slight increase of 180° domain wall motion of the <100> domains is indicated by the ΔN_{100} rising slowly with the applied field, while at 90° ΔN_{100} is zero. The minor rise of $|N_{100}- N_{010}|$, $|N_{100}- N_{001}|$ and continuous increase of N_{010} and N_{001} evidence 90° wall motions, resulting in a relatively low slope in the curve. As the field increases, the increasing of N_{010} and N_{001} and the decrease of N_{100} indicate the domains of <100> flip to <010> and <001>. Thus 90° wall motion becomes dominant, facilitating the reorientation of domains towards the N_{010} and N_{001} and steepening the curve. Beyond H_{c2}, the contribution from domain rotation increases significantly, causing the curve to plateau again.

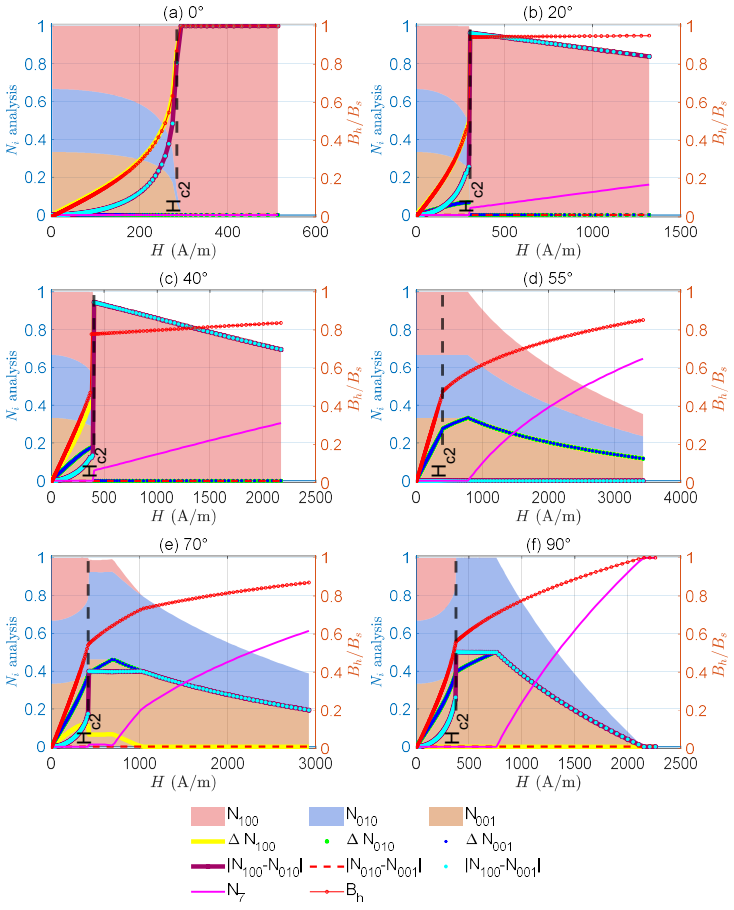

Fig.6. The calculated evolution of magnetization mechanisms under the various excitation conditions.

Fig. 7 presents a comparison between the predicted effective magnetic permeability and the experimental data in a series of directions. The effective permeability μ_e is defined as:

$$\mu_e = \frac{B_h}{\mu_0 H}, \tag{13}$$

The results indicate that the proposed model effectively captures the anisotropic behavior of magnetic permeability. At low field, as shown in Fig.7 (b), the model exhibits lower

prediction accuracy. This is mainly because Model I does not account for the influence of residual stress associated with the coating, which significantly affects the magnetic properties of materials in low field regions [21]. As a result, the parameters μ_1, μ_3, and μ_5 in (7) may become unequal, indicating that the easy axes of the cubic crystal lose their symmetry. Therefore, the deviations between the model predictions and experimental data are more pronounced under low field conditions. At higher fields, the effects of crystallographic texture outweigh that of the stress. Therefore, the present model considering the crystallographic textures can accurately predict the anisotropy. While the present work focuses on single-crystal results, it does not yet account for residual stress or polycrystalline averaging, which limits its quantitative accuracy compared with experimental data. Nevertheless, the proposed model can be extended to polycrystalline steels by incorporating the orientation distribution function, enabling the characterization of both local and global anisotropy for typical textures, and offering potential applicability in practical finite element analysis through an effective permeability tensor.

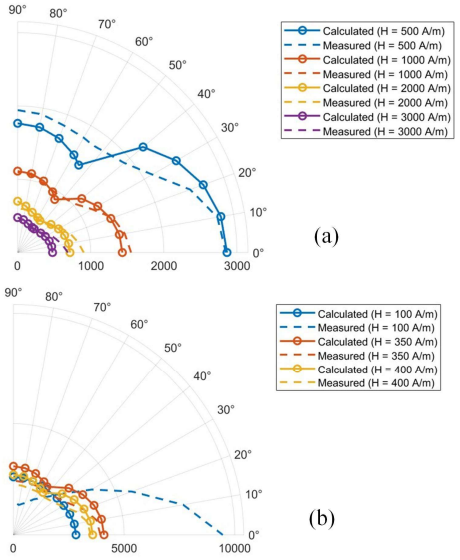

Fig.7. Predicted permeability at various angles relative to RD.

IV. Conclusion

A vector anhysteresis magnetization model covering the full range of the applied field is developed to evaluate the magnetic anisotropy of GO electrical steels. The model captures the anisotropy associated with crystallographic texture and is consistent with the measured trends. The model is based on domain theory and quantitatively describes the evolution of elementary domain distributions, where domains align along easy axes under low fields and gradually rotate toward the external field direction under high fields. The predicted domain configurations offer valuable insight into the domain processes and magnetization mechanism.

Acknowledgment

This work is supported in part by the National Natural Science Foundation of China under Grant 52130710, 52407005 and 52507012, in part by the Funds for Creative Research Groups of Hebei Province (No. E2024202298), and in part by the State Scholarships Fund of China No. 202306700014.

References

[1]A. P. S. Baghel, B. S. Ram, K. Chwastek, L. Daniel, S. V. Kulkarni. Hysteresis Modelling of Go Laminations for Arbitrary in-Plane Directions Taking into Account the Dynamics of Orthogonal Domain Walls. Journal of Magnetism and Magnetic Materials. 2016; 418: 14-20.

[2]K. R. Chwastek, A. P. S. Baghel, M. F. de Campos, S. V. Kulkarni, J. Szczyglowski. A Description for the Anisotropy of Magnetic Properties of Grain-Oriented Steels. IEEE Transactions on Magnetics. 2015; 51(12).

[3]J. Yin, S. Yue, Y. Li, M. Yang, J. Gao, K. Qin. Generalized Fixed-Point Iteration Technique for Solving Magnetic Hysteresis Problems. IEEE Transactions on Industry Applications 2025: 1-11.

[4]B. Upadhaya, P. Rasilo, L. Perkkiö, P. Handgruber, A. Belahcen, A. Arkkio. Comparison of Anisotropic Energy-Based and Jiles-Atherton Models of Ferromagnetic Hysteresis. IEEE Transactions on Magnetics. 2020; 56(4).

[5]R. Y. Chen, F. Martin, Y. J. Li, S. C. Yue, A. Belahcen. An Energy-Based Anisotropic Vector Hysteresis Model for Rotational Electromagnetic Core Loss. IEEE Transactions on Industrial Electronics. 2024; 71(6): 6084-6094.

[6]O. Biró, S. Ausserhofer, K. Preis, Y. Chen. A Modified Elliptic Model of Anisotropy in Nonlinear Magnetic Materials. Compel-the International Journal for Computation and Mathematics in Electrical and Electronic Engineering. 2010; 29(6): 1482-1492.

[7]J. Liu, C. Davis. Tensorial Permeability Microstructure Model Considering Crystallographic Texture and Grain Size for Evaluation of Magnetic Anisotropy in Polycrystalline Steels. Philosophical Magazine. 2021; 101(10): 1224-1244.

[8]J. Liu, C. Davis, S. C. Yue, M. A. Jolfaei, J. L. Shen, Y. J. Li. Scalar Permeability Microstructure Model Considering Crystallographic Texture and Grain Size for Magnetic Evaluation of Anisotropy in Steel. Acta Materialia. 2025; 289.

[9]Y. Li, J. G. Zhu, Y. J. Li, J. Zou, D. Yu. Modeling Magnetostriction of Grain-Oriented Sheet Steels Based on Magnetization Process and Domain Motion. Journal of Magnetism and Magnetic Materials. 2023; 587.

[10] L. Daniel, O. Hubert, N. Buiron, R. Billardon. Reversible Magneto-Elastic Behavior: A Multiscale Approach. Journal of the Mechanics and Physics of Solids. 2008; 56(3): 1018-1042.

[11] O. Hubert, L. Daniel. Multiscale Modeling of the Magneto-Mechanical Behavior of Grain-Oriented Silicon Steels. Journal of Magnetism and Magnetic Materials. 2008; 320(7): 1412-1422.

[12] L. G. Da Silva, A. Abderahmane, M. Domenjoud, L. Bernard, L. Daniel. An Extension of the Vector-Play Model to the Case of Magneto-Elastic Loadings. IEEE Access. 2022; 10: 126674-126686.

[13] S. Ito, T. Mifune, T. Matsuo, C. Kaido. Macroscopic Magnetization Modeling of Silicon Steel Sheets Using an Assembly of Six-Domain Particles. Journal of Applied Physics. 2015; 117(17).

[14] D. Vanoost, S. Steentjes, J. Peuteman, G. Gielen, H. De Gersem, D. Pissoort, et al. Magnetic Hysteresis at the Domain Scale of a Multi-Scale Material Model for Magneto-Elastic Behaviour. Journal of Magnetism and Magnetic Materials. 2016; 414: 168-179.

[15] Y. H. Gao, Y. Eguchi, H. Ebrahimi, H. Dozono, K. Muramatsu, W. M. Guan, et al. Micromagnetics Simulation of Ferromagnetic Materials Using Large Cells. International Journal of Applied Electromagnetics and Mechanics. 2017; 55: S15-S21.

[16] H. Hauser. Energetic Model of Ferromagnetic Hysteresis .2. Magnetization Calculations of (110)[001] Fesi Sheets by Statistic Domain Behavior. Journal of Applied Physics. 1995; 77(6): 2625-2633.

[17] R. M. Bozorth. The Theory of the Ferromagnetic Anisotropy of Single Crystals. Physical Review. 1932; 42(6): 0882-0892.

[18] S. Lee, S. J. Kim. Statistical Analysis of Misorientation to Goss Orientation of Highly Grain-Oriented Silicon Steel. Journal of Magnetism and Magnetic Materials. 2022; 560.

[19] A. D. Rollett, M. L. Storch, E. J. Hilinski, S. R. Goodman. Approach to Saturation in Textured Soft Magnetic Materials. Metallurgical and Materials Transactions a-Physical Metallurgy and Materials Science. 2001; 32(10): 2595-2603.

[20] S. C. Yue, A. J. Moses, P. I. Anderson, C. Harrison, Y. J. Li, Q. X. Yang. Measurement and Analysis of the Non-Symmetry of Transverse Magnetisation and Resulting Loss in Grain-Oriented Steel Using a Modified Rsst. Journal of Magnetism and Magnetic Materials. 2022; 561.

[21] S. W. E. Choby. Evidence for the Effectiveness of Stress Coatings in Improving the Magnetic Properties of High Permeability 3% Si-Fe. IEEE Transactions on Magnetics. 1979; 15(6): 1586 - 1591.